

A Robust and Secure Palm Vessel Biometric Sensing System Based on Photoacoustics

Yuehang Wang, Zhengxiong Li¹, Tri Vu, Nikhila Nyayapathi, Kwang W. Oh, Wenyao Xu², and Jun Xia

Abstract—In this paper, we propose a new palm vessel biometric sensing system based on photoacoustic imaging, which is an emerging technique that allows high-resolution visualization of optical absorption in deep tissue. Our system consists of an ultrasound (US) linear transducer array, an US data acquisition system, and an Nd:YAG laser emitting 1064-nm wavelength. By scanning the array, we could get a 3-D image of palm vasculature. The 3-D image is further combined with our newly developed algorithm, Earth Mover’s Distance—Radiographic Testing, to provide precise matching and robust recognition rate. Compared to conventional vein sensing techniques, our system demonstrates deeper imaging depth and better spatial resolution, offering securer biometric features to fight against counterfeits. In this paper, we imaged 20 different hands at various poses and quantified our system performance. We found that the usability and accuracy of our system are comparable to conventional biometric techniques, such as fingerprint imaging and face identification. Our technique can open up avenues for better liveness detection and biometric measurements.

Index Terms—Photoacoustic imaging (PAI), high-resolution, three-dimensional (3D) image, imaging depth, precise, robust.

I. INTRODUCTION

BIOMETRIC systems allow recognition and verification of an individual through his/her physiological or behavioral characteristics. It is a growing field of research due to the increasing demand for secure and trustworthy authentication systems [2], [3]. Biometrics has vast applications in a variety of fields, such as commercial, personal, and governmental security, as well as forensic investigation. Typical biometric features include fingerprint, face image, iris patterns, and palm vessels. In this paper, we focus on palm vein biometrics. Physiologically, palm veins are a collection of blood vessels in the palm, and they have a complex physical distribution, such as geometry, principal line, and delta point. This structural

Manuscript received April 27, 2018; accepted May 23, 2018. Date of publication June 1, 2018; date of current version June 26, 2018. This work was supported in part by grants from the National Science Foundation and the Center for Identification Technology Research (NSF-CITeR) under Grant No. 1266183, National Science Foundation (Grant No. 1718375), and the Center of Excellence in Materials Informatics. The associate editor coordinating the review of this paper and approving it for publication was Dr. Ioannis Raptis. (Corresponding author: Jun Xia.)

Y. Wang, T. Vu, and J. Xia are with the Department of Biomedical Engineering, University at Buffalo, The State University of New York, Buffalo, NY 14260 USA (e-mail: junxia@buffalo.edu).

Z. Li and W. Xu are with the Department of Computer Science and Engineering, University at Buffalo, The State University of New York, Buffalo, NY 14260 USA.

N. Nyayapathi and K. W. Oh are with the Department of Electrical Engineering, University at Buffalo, The State University of New York, Buffalo, NY 14260 USA.

Digital Object Identifier 10.1109/JSEN.2018.2843119

TABLE I
COMPARISON BETWEEN PAI WITH IR AND US
IN PALM VEIN RECOGNITION

	PAI	US	IR
Vessel contrast	Optical absorption	Doppler shift	Optical absorption
3D capability	Yes	Yes	No
Spatial resolution	Around 0.3 mm in our study	Similar to PAI	Approximately 1 to 3 mm depending on depth.
Imaging depth	Up to 2.7 cm [1]	Similar to PAI	3-4 mm at 850 nm wavelength [2]

complexity in 3D offers stable, distinct, and reliable biometrics for personal identification, and it has a wealth of differentiating features that are unique to each individual [3], [4]. Moreover, unlike fingerprint and facial recognition, vascular structure lies underneath the human skin, which makes the features very difficult to counterfeit. Owing to these unique properties, palm veins are ideal for biometric authentication.

Existing work on palm-view imaging techniques mainly focused on ultrasound (US) or infrared (IR) optical imaging [4]–[6]. However, these techniques have inherent limitations. For instance, Doppler ultrasound measures the Doppler shift generated by blood flow, and the technique is sensitive to only large vessels due to the presence of more Rayleigh scatters (red blood cells) [7]. However, the sparse large vessel map barely satisfies the requirement of accuracy and security in biometric applications. As for vein patterns acquired from infrared optical imaging, they contain no information about vessel depth. The diffuse nature of light also significantly degrades the image quality, generating blurry vascular images. Furthermore, these systems are based on two-dimensional (2D) feature matching, which is vulnerable to forge.

As a growing technique, photoacoustic imaging (PAI) has great potential for biometric applications. However, existing works on PAI-based biometrics are all for fingerprint imaging [8], [9], which does not exploit the full potential of PAI—high resolution imaging in deep tissue. Here, to overcome limitations of traditional palm vessel imaging techniques, we develop a highly accurate and robust biometric system based on this advanced imaging modality. In Table I, we compare PAI with other palm vessel imaging techniques. PAI and ultrasound share similar spatial resolution. However, unlike Doppler ultrasound which depends on the Doppler shift,

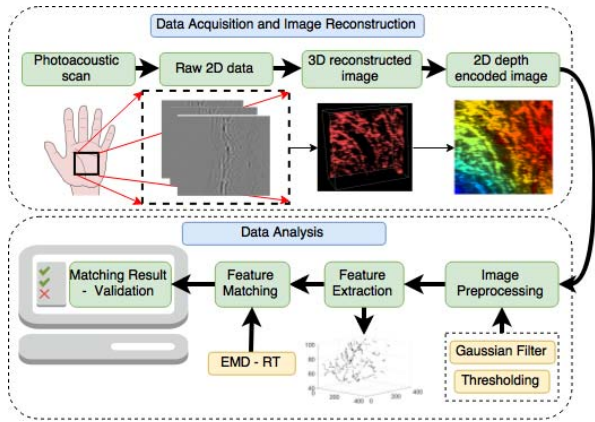


Fig. 1. Overview of the photoacoustic palm vessel biometrics.

PA signals originate from optical absorption of red blood cells, and thus it provides much higher vascular contrast. In comparison to infrared optical imaging, PAI breaks through the optical diffusion limit, allowing high resolution, three-dimensional (3D) visualization of the vasculature, which is more complex, distinct, and hence securer. Overall, the high contrast and 3D information offered by PAI can easily overcome the limitations of conventional methods.

Along with the PAI system, we also developed a robust and advanced 3D vessel matching algorithm, Earth Mover's Distance-Radiographic Testing (EMD-RT), to effectively match the palm vessel distribution in 3D space. In detail, EMD-RT is human physiology specific and in opposition to rigid transformation in practical usage. Overall, our solution comprehensively addresses two main concerns for traditional hand vessel biometrics: 3D representation and hand pose.

An overview of the system is shown in Fig. 1. The first step is to scan the object and acquire data. Principle of photoacoustic imaging is presented in Section II, the study design is discussed in Section III, and the system hardware and software are introduced in Section IV. In Section V, we describe image preprocessing and feature extraction methods. The final step is to use our EMD-RT method to perform feature matching. Details of this method are described in Section VI. In the end, we verify our approach in terms of accuracy and usability.

II. PHOTOACOUSTIC IMAGING

A. Background

The photoacoustic (PA) effect was first discovered by Bell [10], when he realized that sound waves were produced when modulated sunlight was focused on a solid sample. The development of lasers in the 1960s triggered the rapid advancement of research in the area of photoacoustics. Currently, photoacoustics has become the most exciting biomedical imaging technique in this decade [11]. The PA effect is observed when short-pulsed electromagnetic radiation is used as an excitation source. Due to photon absorption and thermoelastic expansion in the sample, ultrasound signals are generated. Because acoustic scattering in tissue is much less than that of light, the conversion of light into sound allows PAI

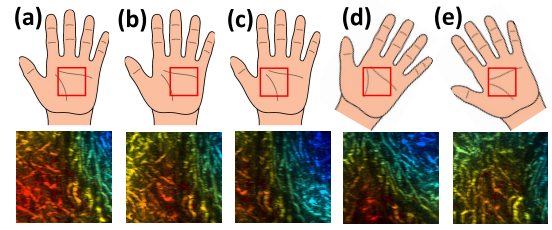


Fig. 2. Five different poses for each palm imaging experiment: (a) standard, (b) move to the left (~ 1 cm), (c) move to the right (~ 1 cm), (d) rotate clockwise (~ 30 degrees), and (e) rotate counterclockwise (~ 30 degrees). Red solid boxes show the region of interest (ROI). The top row shows schematic illustration while the bottom row shows corresponding depth-encoded photoacoustic images.

to break through the optical diffusion limit and reveal optical absorption deep inside tissue, with high spatial resolution. Over the past few years, applications of PAI have expanded rapidly, ranging from small-animal imaging to clinical cancer imaging [12]–[16].

B. Photoacoustic Imaging Principle

Upon irradiation by a short-duration laser pulse, the object will experience transient thermoelastic expansion, which leads to wideband ultrasonic emission. Typical pulsed laser sources used in PA have a pulse width of a few nanoseconds, which is lower than both the thermal and stress confinements [17]. The photoacoustic pressure (p_0) can be defined by the following equation:

$$p_0(\vec{r}) = \Gamma \mu_a F(\vec{r}), \quad (1)$$

where $F(\vec{r})$ is the local optical fluence, μ_a is the absorption coefficient and Γ represents the Grueneisen parameter which increases linearly with temperature [18]. The induced acoustic waves are then detected by ultrasonic transducers. Distribution of optical absorption can be obtained by back-projecting the detected signals [19]–[22]. Since ultrasound scattering in tissue is very weak in comparison to optical scattering, PAI allows for high-resolution imaging of optical absorption in deep tissue.

III. STUDY DESIGN

In this study, 10 volunteers with ages ranging from 20 to 40 years were recruited. We imaged both right and left palms for each volunteer, resulting in a total of 20 palms. Each palm was imaged at 5 different poses: (i) standard, (ii) move to the right (~ 1 cm), (iii) move to the left (~ 1 cm), (iv) rotate clockwise (~ 30 degrees), and (v) rotate counterclockwise (~ 30 degrees). Different poses of a palm and corresponding photoacoustic images are shown in Figure 2. All human imaging procedures were performed in compliance with the University at Buffalo IRB protocol. After collecting PAI biometric samples, the identification process involves preprocessing the data, extracting the biometric feature, matching templates, and finally recognizing the user. Since infrared optical imaging is a mature and commonly used technique for palm vein visualization [23]–[26], we also acquired infrared vein images to compare with our PAI results.

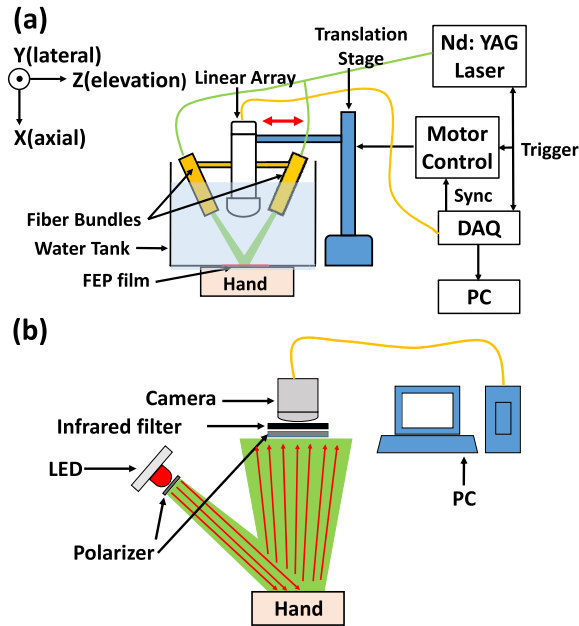


Fig. 3. System schematics. (a) The photoacoustic imaging system. The red double arrows indicate the scanning direction. (b) The infrared vein visualization system.

IV. PHOTOACOUSTIC IMAGING AND INFRARED VEIN VISUALIZATION SYSTEMS

A. PAI System

Fig. 3(a) shows a schematic of the PAI system. The system consists of three main components: a 10-ns-pulsed Nd:YAG laser with 10 Hz pulse repetition rate and 1064 nm output wavelength, an ATL L7-4 transducer array with 5 MHz central frequency and 128 elements, and a Verasonics' Vantage 128 data acquisition system with 128 receive channels.

Although Hb and HbO₂ have absorption peaks in the visible light regime, the imaging depth is quite limited at these wavelengths. Hence, for the PAI biometric system, we used a wavelength of 1064 nm, which provides a few centimeters penetration in tissue. The output from the 1064 nm laser was coupled into a bifurcated fiber bundle with 1.1-cm-diameter circular input and two 5.1-cm-length line outputs (Schott Fostec). The two line outputs were attached to the ultrasound transducer with a lab-made mount. For better subject positioning, we designed an open-bottom water tank and submerged both the transducer and optical fiber outputs in water. The bottom of the water tank was sealed with 0.05 mm thickness fluorinated ethylene propylene (FEP) plastic film (McMASTER-Carr), so that the object could be imaged through this window. During the experiment, the distance between the transducer and the hand was fixed to 25 mm (focal length of the L7-4 transducer). Ultrasound gel was applied to couple the FEP film and hand.

As for laser safety, the output energy of our laser is 680 mJ/pulse. The coupling efficiency of the fiber bundle is around 60%, so that only ~ 408 mJ of laser power will be emitted from the fiber output. The size of the laser beam on the object's surface was measured to be approximately $2.5 \text{ cm} \times 6.0 \text{ cm}$ (15 cm^2). Therefore, the light intensity on

skin surface is 27 mJ/cm^2 ($408 \text{ mJ}/15\text{cm}^2$), which is much lower than the safety limit of 100 mJ/cm^2 at 1064 nm [27].

For each subject, we scan the transducer over 40 mm distance, covering an area of 38 mm (lateral length of the transducer) by 40 mm. To avoid operator dependence, motorized scanning was applied instead of freehand scanning. At 0.1 mm step size, one experiment takes 40 seconds. This imaging time can be significantly shortened by utilizing a higher speed laser [28]. Following PAI data collection, we employ the universal back project algorithm [22] to reconstruct a vascular image from the raw channel data. All reconstructed 2D images are then stacked, based on the scanning direction, to form a 3D image of palm vasculature. In this study, we didn't perform direct 3D reconstruction because it is more susceptible to hand movement and needs a longer reconstruction time.

B. Infrared Vein Imaging System

The infrared vein visualization system (Fig. 3b) consists of an infrared LED (Vastfire, IR-A100, 850 nm, bandwidth 810nm-1110nm), a CCD camera (Basler scA1390-17gm GigE), an infrared filter (Neewer IR760 52 mm), which passes infrared rays above 760 nm, and two optical linear polarizers (Thorlabs, LPNIRE200-B). The infrared filter removes the ambient visible light, while the two polarizers are installed orthogonally (one in front of the laser and the other in front of the camera) to remove light reflection from the skin. The light intensity on the skin surface was approximately 12 mW/cm^2 , which is much lower than 400 mW/cm^2 , the maximum permissible exposure intensity limit [27].

IR vein imaging is based on the following principle: (a) infrared light will penetrate through the skin and get absorbed by red blood cells; (b) after multiple scattering events, some photons will re-emit out of the skin; (c) strong absorption from blood vessels will create a shadow in the backscattered image. Thus, blood vessels are visualized as negative contrasts in the camera. Conversely, the PAI system exhibits blood vessels as positive contrasts.

C. Comparison of PAI and Infrared Vein Imaging Systems

To validate the performance of PAI and infrared vein visualization systems, we first imaged a tube with 1 mm inner diameter. The tube was filled with black ink and was embedded near the top surface of an agar gel (containing 3% of agar by weight), which mimics optical scattering in tissue [29], [30]. As shown in Fig. 4(a), the tube is twisted to mimic vascular structures. We then cover the phantom with a piece of 5-mm thick agar gel and image it with the infrared vein visualization system. As shown in Fig. 4(b), the tube structure looks very blurry. In comparison, the photoacoustic image (Fig. 4c.) clearly shows the tube at different depths. Along the red solid lines in Fig. 4(b) and 4(c), we quantified the full-width half maximum (FWHM) to be 2.3 mm and 1.1 mm, respectively. The signal to noise (SNR) is 67 and 97 for IR and PAI, respectively. The tube phantom result demonstrated that the PAI system indeed provides a better spatial resolution and SNR than that of the infrared vein visualization system.

Figure 5 shows PAI and IR images of the same palm. As shown in Fig. 5(a), an area of $3.8 \text{ cm} \times 4 \text{ cm}$ (yellow box)

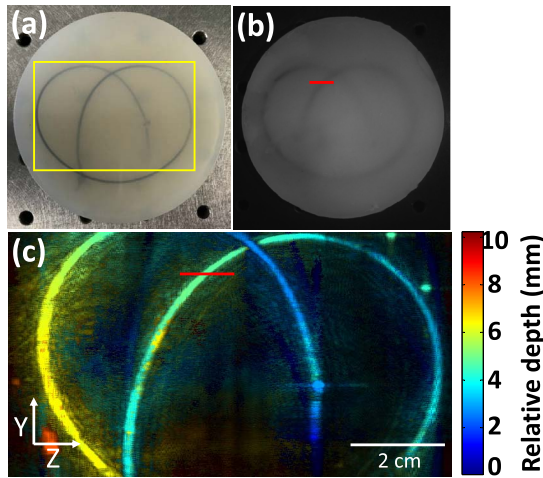


Fig. 4. Comparison of tube phantom imaging by PAI and IR techniques. (a) Photograph of the tube phantom. (b) IR image of the tube phantom covered by agar gel. (c) Depth-encoded photoacoustic image of the tube phantom in (b). Yellow boxes indicate the ROI. Red solid lines indicate the cross section for the FWHM quantification.

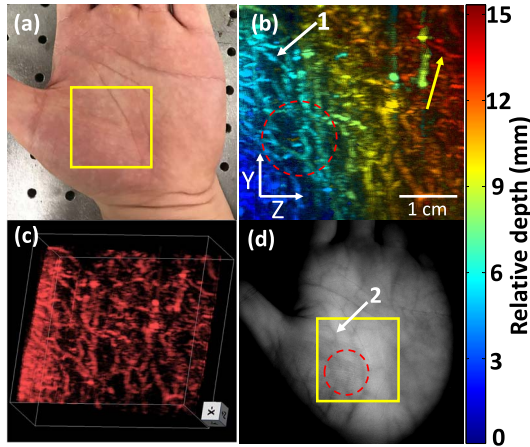


Fig. 5. Comparison of palm vessel imaging by PAI and IR techniques. (a) Photograph of the palm of a volunteer. (b) Depth-encoded vascular image of the palm in (a). The yellow arrow points to the smallest vessel in the image. (c) A 3D rendering of the image in (b). (d) IR image of the same palm. Yellow boxes indicate the ROI. Red dashed circles highlight a vessel branch that is visible in both in (b) and (d). White arrows point to the same vessel used for resolution quantification.

was imaged by both PAI and IR systems. Fig. 5(b) and 5(c) shows the depth-encoded maximum intensity projection (MIP) PA image and 3D rendered PA image, respectively. From both images, rich vascular structures can be clearly revealed. This result indicates that the PAI technique can clearly resolve features distributed over 15 mm in depth. The IR image is shown in Fig. 5(d), with a yellow box marking the same region of PAI. It can be seen that blood vessels are very blurry within the yellow box. Even though the IR result is quite blurry, we were able to locate a few common features in both PAI and IR images, as indicated by red circles. To quantify the spatial resolution, we calculated the full-width half maximum (FWHM) of the same vessel as pointed by white arrows in both PAI and IR results. The resolution is 0.7 mm and 1.8 mm for PAI and IR results, respectively. The PAI resolution agrees with the theoretical estimation of 0.3 mm along the y-axis and 1.5 mm along the z-axis (the vessel

is not parallel to either axis, thus the cross section width is determined by resolutions along both axes). The smallest vessel of the PAI result is pointed by a yellow arrow. The same vessel cannot be seen in Fig. 5d. In terms of vessel density, for the same ROI, it is obvious that PAI vascular structures are denser than those in the IR image. Additionally, unlike PAI result, IR only provides a 2D image, and there is no depth information about the vasculature. The depth of vessels detected by PAI provides liveness information of the subject, which is difficult to counterfeit. Thus, our PAI biometric system is much securer than the 2D IR system.

V. IMAGE PREPROCESSING AND FEATURE EXTRACTION

In this section, we describe details about PA image preprocessing and feature extraction. This step is critical to achieving better performance in our system. As shown in Figure 1, there are two tasks in this process. First, we develop a preprocessing algorithm to obtain vascular structures from the PA image. Second, we extract fiducial points to represent biometric features in each palm. Feature extraction will allow us to construct the topology of hand vessels and subsequently, improve the robustness and efficiency of biometric matching.

The first step of image preprocessing is to utilize a Gaussian filter to remove high-frequency noises in the system [31]. Next, we will extract vascular structures through image binarization. Currently, there are many other methods that can extract vascular features from the background [31]–[33]. Computed Tomography (CT) and Magnetic Resonance Imaging (MRI) sensing usually get the blood flow based on the blood flow edge or centerline. They first locate the blood flow area and then achieve the segmented vessel structure using filter-based or cluster-based approaches. When it comes to PAI, we utilize binarization because PAI has high vascular contrast. Binarization is the process of converting a grayscale image to a binary image, which is a digital image that has only two possible values for each pixel. Thus, the vessel segment is the process of assigning each pixel in the source image to two classes. The global threshold for binarization is defined after analyzing histograms of the images. If the grayscale value of a pixel is higher than the threshold, this pixel is regarded as the vascular portion and reset the grayscale value to 255. If its value is lower than the threshold, it is treated as the background and its grayscale value is set to 1. Finally, the vascular structure is extracted from the background. This preprocessing approach is computationally very lightweight and it also reduces the processing time, enabling real-time data processing.

As for feature extraction, we need to track the flow of blood vessels among 3D slices/images to establish the vessel structure. Because the receiving sensitivity and spatial resolution of PAI vary depending on the vessel direction, some vessels may appear disconnected in the 3D image. In order to repair these broken vessels and form a complete digital signature for feature matching, we deploy Nearest Neighbor Search. It is a form of proximity search and is an optimization problem of finding the point in a given set that is closest (or most similar) to a given point. This search is simple to

implement and flexible to distance choices. It finds and links the next vessel point in a given set that is the most similar to a given vessel. Its working mechanism is represented in the following: $\|x - x_i\| = \arg \min \sqrt{\sum_j (x_j - x_{ij})^2}$, where x is the coordination of a new point and x_i is its next connecting point. It follows the strategy of keeping track of the “best so far” [34], [35].

After this procedure, we obtain an initial vessel set. However, there is still much redundancy in vein topology and it is still not easy to find features for vein matching. To refine the vessel and extract features, we select the skeleton-based marching cubes method [34]. It categorizes points of extracted vessels with the smallest distance based on the number of neighboring background points and then erase points in descending order of the number of neighboring background points. Finally, it implements a post-processing technique to remove obviously false positive detected vessel bifurcations based on their proximity to an end-point. Compared to other vascular structure reconstructions [36], [37], this method is easily deployed and invariant to a rotation. In addition, it has the least lightweight computing consumption and high accuracy. Although it requires a rotation invariant algorithm for matching, this constraint is satisfied by the vascular feature matching algorithm in the following section. After refining the vascular structure, we find two most basic features in the vascular structure: zigzag and bifurcation. Based on the vessel theory, zigzag ensures more blood to be stored within a confined region, while bifurcation is where a vessel diverges to form new vessels or capillaries [38].

VI. MATCHING ALGORITHM: EMD-RT

In this part, we introduce the proposed matching algorithm, which accounts for variations in hand rotation and poses. Our previous procedures convert each input image into feature sets. These feature sets can be compared with the genuine template in the database to verify their legitimacy.

Currently, Euclidean, Hamming, and Hausdorff distances are widely used in biometric matching. In particular, the Euclidean distance was used with hand geometry [39], the Hamming distance was applied in fingerprint-iris research [40], and the Hausdorff distance could be found in palm print detection [41]. Euclidean and Hamming distances are applied in 1-to-1 matching, while the Hausdorff Distance is used in 1-to-N matching. Unlike hand geometry, fingerprint, iris, or palm print, in which biometric features will not change, the palm vessels could have significant deformation due to its physical characters [38]. It is highly possible that two compared vein feature sets possess different sizes, leading to M-to-N matching. Thus, those previous matching approaches may not work for our study.

Definition: We present the vascular structure in terms of clusters. Each cluster is a single point in three dimensions. The weight of the cluster is decided by the fraction of vessel distribution presented in that cluster. A set of clusters is called the signature. The signatures can have different sizes. One cluster can be considered as a single feature in a signature. The distance between two features is named as the ground

TABLE II
THE DEFINITION OF VARIABLES IN EMD-RT

Variables	Definition
A cluster	A single point in multi dimensions
The weight of a cluster	The fraction of vessel distribution present in that cluster
A signature	A set of clusters
A feature	One cluster
The ground distance	The distance between two features
Matching points	A pair of features with the least distance

distance. The shorter the ground distance, the higher similarity of two features. A pair of features with the least distance is considered as the matching sets. Definition of variables is listed in Table II.

Formulation: Given two vascular structures A and B in dimension three. Structure A is an input and Structure B is the genuine template. Assuming Structure A is constituted by m clusters, it can then be represented as Signature $A = \{(p_1, w_{p_1}) \cdots (p_m, w_{p_m})\}$, $1 \leq i \leq m$, where p_i is the cluster representative and w_{p_i} is the weight of the cluster. Similarly, Structure B can be represented as Signature $B = \{(q_1, w_{q_1}) \cdots (q_n, w_{q_n})\}$, $1 \leq j \leq n$. Then, we define $D = [d_{ij}]$ to be the ground distance between clusters p_i and q_j with $d_{ij} = \|p_i - q_j\|$. In the EMD-RT model, the transformed cluster q'_i is satisfied with $q'_i = Mq_i + C$, where M is the rotation matrix and C is the translation matrix. At the same time, d'_{ij} is bounded up to δ , i.e., $d'_{ij} = \|p_i - q'_j\| < \delta$. Thus, we aim to find the minimum directional distance between two features. The directional distance is defined as flow $F = [f_{ij}]$, where f_{ij} is the flow between p_i and q'_j . The flow represents the corresponding (or alignment) information between p_i and q'_j .

$$\begin{aligned} \text{Minimize } EMD - RT(A, B, F) &= \frac{\sum_{i=1}^m \sum_{j=1}^n f_{ij} d'_{ij}}{\sum_{i=1}^m \sum_{j=1}^n f_{ij}} \\ \text{s.t. } f_{ij} &\geq 0, \quad 1 \leq i \leq m, \quad 1 \leq j \leq n \\ \sum_{j=1}^n f_{ij} &\leq w_{p_i}, \quad 1 \leq i \leq m \\ \sum_{i=1}^m f_{ij} &\leq w_{q_j}, \quad 1 \leq j \leq n \\ \sum_{i=1}^m \sum_{j=1}^n f_{ij} &= \min\left(\sum_{i=1}^m w_{p_i}, \sum_{j=1}^n w_{q_j}\right) \end{aligned} \quad (2)$$

Our algorithm includes the following constraints: 1) limits the matching direction, allowing moving “supplies” from Signature A to Signature B and not vice versa; 2) limits the amount of supplies that can be sent by the clusters in Signature A to their weights; 3) limits the clusters in Signature B to receive no more supplies than their weights; 4) forces to move the maximum amount of supplies possible [42].

We formulate the problem of authentication as matching between two vascular structures, which may have unequal length, deformation, and rotation. EMD is a measure of the distance between two probability distributions over a

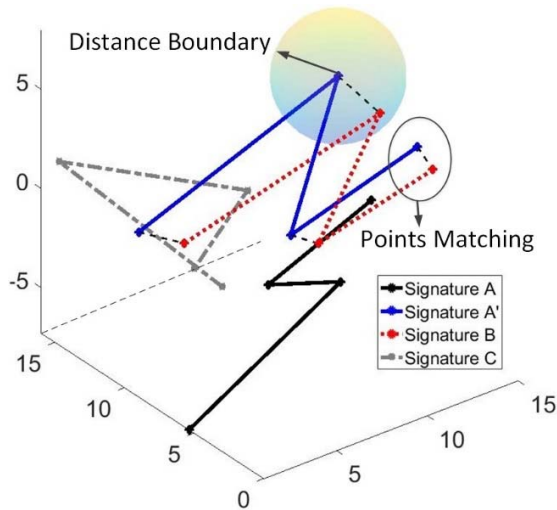


Fig. 6. Earth Mover's Distance-Radiographic Testing (EMD-RT) illustration.

region [38], [43], [44]. It is suitable for vascular structure matching, because of the following three reasons: 1) hand vein topology is essentially the movement of corresponding points on the image, which naturally fits the principle of EMD, 2) N-to-M EMD matching is adaptive to variations in feature numbers, and 3) compared to other distance metrics [45]–[47], EMD has a better tolerance to deformation in matching. Our study employs an extended Earth Mover's Distance for Radiographic Testing (EMD-RT), by enhancing two particular aspects. First, we assume the boundary matching distance to be δ , and no matching pair distance could be larger than δ . This constraint is set because palm vein physical characteristics stay relatively constant regardless of the hand pose [48] and the palm vessel diameters expand between 0.5 to 0.9 mm [4]. Therefore, geometric deformation should be limited to a certain range due to human physical constraints and matching points should be within the distance boundary. Second, because the hand pose could change in each experiment, our algorithm takes into account of hand rotation.

In practice, we compare all features against the corresponding template features. For illustration, Figure 6 shows a matching result of two feature sets in vascular structures. For vasculatures, zigzag and bifurcation are the most common basic features. In Figure 6, Signature A and B are zigzag, while Signature C looks like bifurcation, implying that Signature A is matched with Signature B and both are quite different from Signature C. Under EMD-RT metric, Signature A first rotates with a proper angle into Signature A' and then matches with Signature B at each point. After the normalization, EMD-RT distance between Signature A and Signature C is 3 times larger than the distance between Signature A and Signature B, which matches with our observation. However, under Euclidean, Hamming and Hausdorff approaches, the distance between Signature A and Signature B could be equal or even larger than the distance between Signature A and Signature C, leading to erroneous judgment. Therefore, our proposed EMD-RT algorithm is more robust for this application. Also, it is worth mentioning that the EMD-RT algorithm can also be applied to the 2D IR images or other sensing systems for vein matching.

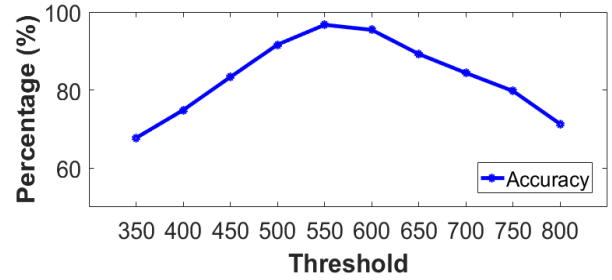


Fig. 7. The system accuracy at different threshold values.

TABLE III
THE OVERALL SYSTEM PERFORMANCE

Evaluation Index	Result (%)
False acceptance rate	0.51
False rejection rate	1.72
Equal error rate	1.93

VII. VALIDATION PROTOCOL

After vein matching, we get a scalar measurement result. In order to validate this system, after collecting the sample templates, we conduct the following analyses. To evaluate the overall performance, we compare test palm veins against their corresponding templates. Only when the EMD-RT matching result is less than a pre-defined threshold, the PA test palm vein will be considered as being acquired from the same volunteer, the pre-registered genuine one. Here, the threshold value selection is a crucial factor for biometric system. As shown in Fig. 7, we quantified the accuracy of the system under different thresholds from 350 to 800 and found that the accuracy reaches the highest when the threshold was between 550 and 600. Finally, we set the threshold at 570 for our system. For robustness and usability test, we employ ten individuals scanning their hands with five different hand poses as templates. Similarly, after getting these samples, we test palm veins to verify whether the system works under all conditions.

VIII. RESULTS

We also evaluated the overall performance in terms of false acceptance rate (FAR), false rejection rate (FRR), and equal error rate (EER) (Table III). FAR measures the likelihood that the biometric security system will incorrectly accept an access attempt by an unauthorized user. FRR measures the likelihood that the biometric security system will incorrectly reject an access attempt by an authorized user. The EER value indicates that the proportion of false acceptances is equal to the proportion of false rejections. In this system, we achieve an EER of 1.93%, which indicates that our proposed template creation method is feasible and effective for palm vein recognition with high accuracy. In comparison, the IR imaging study reported in [5] reported an EER of 4.2%. We also calculated the Receiver Operating Characteristics (ROC) curve as shown in Fig. 8. The area under the ROC curve (AUC) is used as the optimization objective since it provides a good representation of the ROC performance. In this system, the AUC value is 97.18%, which shows that our classification method is extremely good.

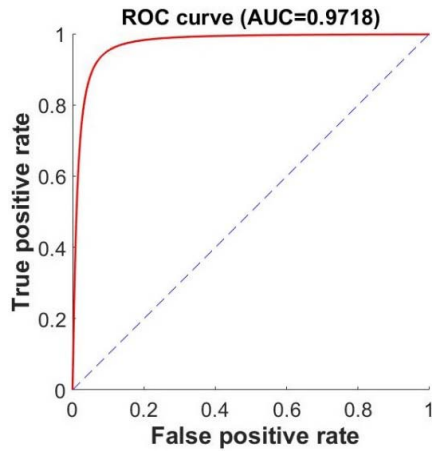


Fig. 8. The ROC curve of system overall performance with standard hand pose.

TABLE IV
THE ROBUSTNESS PERFORMANCE

Pose	Accuracy Result (%)	Variation (%)	Average Time (s)
Standard	99.31	±0.3	1.13
Move to left	99.13	±0.5	1.44
Move to right	99.15	±0.4	1.48
Rotate clockwise	99.05	±0.8	1.87
Rotate counterclockwise	99.07	±0.9	1.93

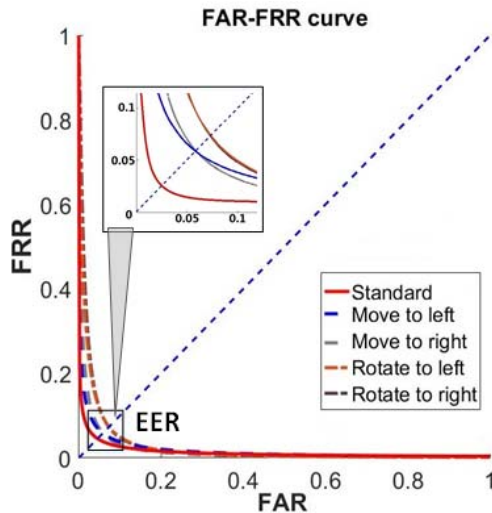


Fig. 9. ROC curves of different hand poses.

As for robustness and usability tests, we conduct an experiment to scan the user's palm vein in five different ways: (i) standard, (ii) move to left, (iii) move to the right, (iv) rotate clockwise, and (v) rotate counterclockwise. Data in Table IV shows that our system works successfully with different hand poses. For all cases, the accuracy is higher than 99%, variation is less than 1%, and execution time is less than 2 seconds. The FAR-FRR curve in Fig. 9 indicates that the EERs for all 5 different hand poses are less than 8%. This result shows that the system works very well for different hand poses, offering great usability. In fact, the usability of our system

is comparable to conventional authentication methods, such as fingerprint.

IX. CONCLUSION

In summary, we have successfully developed a reliable and robust 3D PAI palm vessel biometric sensing system for personal identification. Compared to existing IR and ultrasound based palm-vessel imaging techniques, our system provides better spatial resolution and imaging depth. Compared to PAI based fingerprint biometric systems, our system relies on 3D structures. The addition of depth information makes it securer than 2D fingerprint mapping. In the future, multiple wavelengths can be used to measure the hemoglobin oxygen saturation to further improve the liveness detection capability.

We have also proposed a new algorithm EMD-RT for matching of vascular features. In our palm vessel template of 100 palm vein images from 20 different palms, we could achieve a high recognition rate (more than 99%), with a corresponding error rate of 1.93%, which is comparable or superior to all other hand-based biometrics, such as hand geometry, palm vein imaging, and fingerprint verification [5], [41], [47], [49]. Moreover, it is extremely tolerant to hand movement and pose, indicating high robustness and usability of the system. In the current system, we utilized a relatively bulky laser to acquire PA images. In the future, we can apply high-speed light-emitting diode (LED) or laser diodes as light sources to reduce the size of our system and increase the imaging speed [50]–[52]. In addition, instead of linear transducer arrays, we can utilize a 2D ultrasound transducer array to eliminate the need for translational scanning. In terms of matching speed, if we continue optimizing the 3D vessel model and pruning less significant vascular features, the total matching time would be reduced to millisecond scale, achieving real-time identification. With an increasing demand for securer biometric techniques, we believe that our method will find great applications in different areas.

REFERENCES

- [1] M. Toi *et al.*, "Visualization of tumor-related blood vessels in human breast by photoacoustic imaging system with a hemispherical detector array," *Sci. Rep.*, vol. 7, Feb. 2017, Art. no. 41970.
- [2] Y. Zhou and A. Kumar, "Human identification using palm-vein images," *IEEE Trans. Inf. Forensics Security*, vol. 6, no. 4, pp. 1259–1274, Dec. 2011.
- [3] P. L. Hawkes and D. Clayden, "Veincheck research for automatic identification of people," in *Hand Fingerprint Seminar at NPL*. London, U.K., 1993, pp. 230–236.
- [4] J.-C. Lee, "A novel biometric system based on palm vein image," *Pattern Recognit. Lett.*, vol. 33, no. 12, pp. 1520–1528, 2012.
- [5] R. R. Fletcher *et al.*, "Development of mobile-based hand vein biometrics for global health patient identification," in *Proc. IEEE Global Humanitarian Technol. Conf. (GHTC)*, Oct. 2014, pp. 541–547.
- [6] A. Iula, A. Savoia, and G. Caliano, "3D Ultrasound palm vein pattern for biometric recognition," in *Proc. IEEE Int. Ultrason. Symp. (IUS)*, Oct. 2012, pp. 1–4.
- [7] T. R. Nelson and D. H. Pretorius, "The Doppler signal: Where does it come from and what does it mean?" *Amer. J. Roentgenol.*, vol. 151, no. 3, pp. 439–447, 1988.
- [8] K. Song *et al.*, "Photoacoustic and colorimetric visualization of latent fingerprints," *ACS Nano*, vol. 9, no. 12, pp. 12344–12348, 2015.
- [9] W. Y. Choi and K. K. Park, "Fingerprint imaging of dry finger using photoacoustics," *J. Acoust. Soc. Amer.*, vol. 141, no. 3, pp. EL205–EL209, 2017.
- [10] A. G. Bell, "Upon the production and reproduction of sound by light," *J. Soc. Telegraph Eng.*, vol. 9, no. 34, pp. 404–426, 1880.

- [11] S. Manohar and D. Razansky, "Photoacoustics: A historical review," *Adv. Opt. Photon.*, vol. 8, no. 4, pp. 586–617, 2016.
- [12] Y. Wang, D. Wang, R. Hubbell, and J. Xia, "Second generation slit-based photoacoustic tomography system for vascular imaging in human," *J. Biophoton.*, vol. 10, nos. 6–7, pp. 799–804, 2017.
- [13] R. A. Kruger, C. M. Kuzniak, R. B. Lam, D. R. Reinecke, S. P. D. Rio, and D. Steed, "Dedicated 3D photoacoustic breast imaging," *Med. Phys.*, vol. 40, no. 11, p. 113301, 2013.
- [14] C. P. Favazza, L. V. Wang, O. W. Jassim, and L. A. Cornelius, "In vivo photoacoustic microscopy of human cutaneous microvasculature and a nevus," *J. Biomed. Opt.*, vol. 16, no. 1, pp. 016015-1–016015-6, 2011.
- [15] E. Zhang, J. G. Laufer, R. B. Pedley, and P. C. Beard, "In vivo high-resolution 3D photoacoustic imaging of superficial vascular anatomy," *Phys. Med. Biol.*, vol. 54, no. 4, p. 1035, 2009.
- [16] Y. Wang, D. Wang, Y. Zhang, J. Geng, J. F. Lovell, and J. Xia, "Slit-enabled linear-array photoacoustic tomography with near isotropic spatial resolution in three dimensions," *Opt. Lett.*, vol. 41, no. 1, pp. 127–130, 2016.
- [17] L. V. Wang, "Tutorial on photoacoustic microscopy and computed tomography," *IEEE J. Sel. Topics Quantum Electron.*, vol. 14, no. 1, pp. 171–179, Jan./Feb. 2008.
- [18] L. Wang, J. Xia, J. Yao, K. I. Maslov, and L. V. Wang, "Ultrasonically encoded photoacoustic flowgraphy in biological tissue," *Phys. Rev. Lett.*, vol. 111, no. 20, p. 204301, 2013.
- [19] J. Xia, J. Yao, and L. V. Wang, "Photoacoustic tomography: Principles and advances," *Electromagn. Waves (Cambridge, Mass.)*, vol. 147, pp. 1–22, May 2014.
- [20] L. V. Wang and S. Hu, "Photoacoustic tomography: In vivo imaging from organelles to organs," *Science*, vol. 335, no. 6075, pp. 1458–1462, 2012.
- [21] J. Xia and L. V. Wang, "Small-animal whole-body photoacoustic tomography: A review," *IEEE Trans. Biomed. Eng.*, vol. 61, no. 5, pp. 1380–1389, May 2014.
- [22] M. Xu and L. V. Wang, "Universal back-projection algorithm for photoacoustic computed tomography," *Biomed. Opt.*, vol. 2005, no. 1, pp. 251–254, Jan. 2005.
- [23] R. N. Varma, S. D. Sahane, and S. S. Thankre, "Infrared vein viewer," *J. Eng., Educ. Technol.*, vol. 2, no. 1, pp. 1–2, 2014.
- [24] M. V. Karaaltin, "Utilizing the vein viewer technology to map out a venous flap preoperatively," *J. Reconstruct. Microsurgery*, vol. 29, no. 6, pp. 423–424, 2013.
- [25] K. Phipps, A. Modic, M. A. O'Riordan, and M. Walsh, "A randomized trial of the Vein Viewer versus standard technique for placement of peripherally inserted central catheters (PICCs) in neonates," *J. Perinatol.*, vol. 32, no. 7, pp. 498–501, 2012.
- [26] L. Xueyan and G. Shuxu, "The fourth biometric-vein recognition," in *Pattern Recognition Techniques, Technology and Applications*. London, U.K.: InTech, 2008.
- [27] *American National Standard for the Safe Use of Lasers*, Standard ANSI Z136, American National Standards Institute, New York, NY, USA, 2007.
- [28] D. Wang *et al.*, "Deep tissue photoacoustic computed tomography with a fast and compact laser system," *Biomed. Opt. Express*, vol. 8, no. 1, pp. 112–123, 2017.
- [29] B. W. Pogue and M. S. Patterson, "Review of tissue simulating phantoms for optical spectroscopy, imaging and dosimetry," *J. Biomed. Opt.*, vol. 11, no. 4, pp. 041102-1–041102-16, 2006.
- [30] R. Cubeddu, A. Pifferi, P. Taroni, A. Torricelli, and G. Valentini, "A solid tissue phantom for photon migration studies," *Phys. Med. Biol.*, vol. 42, no. 10, p. 1971, 1997.
- [31] E. C. Lee and K. R. Park, "Image restoration of skin scattering and optical blurring for finger vein recognition," *Opt. Lasers Eng.*, vol. 49, no. 7, pp. 816–828, 2011.
- [32] M. M. Fraz *et al.*, "An approach to localize the retinal blood vessels using bit planes and centerline detection," *Comput. Methods Programs Biomed.*, vol. 108, no. 2, pp. 600–616, 2012.
- [33] C. Yuan, E. Lin, J. Millard, and J.-N. Hwang, "Closed contour edge detection of blood vessel lumen and outer wall boundaries in black-blood MR images," *Magn. Reson. Imag.*, vol. 17, no. 2, pp. 257–266, 1999.
- [34] Y. Sugano, S. Onogi, A. Bossard, T. Mochizuki, and K. Masuda, "Development of a 3D reconstruction of blood vessel by positional calibration of ultrasound probe," in *Proc. Biomed. Eng. Int. Conf. (BMEiCON)*, Dec. 2012, pp. 1–4.
- [35] Z. Wu *et al.*, "3D ShapeNets: A deep representation for volumetric shapes," in *Proc. IEEE Conf. Comput. Vis. Pattern Recognit.*, Jun. 2015, pp. 1912–1920.
- [36] M. Z. Alom, M. Mostakim, R. Biswas, and A. Chakrabarty, "Automatic slice growing method based 3D reconstruction of liver with its vessels," in *Proc. 16th Int. Conf. Comput. Inf. Technol. (ICCIT)*, Mar. 2014, pp. 338–344.
- [37] X. Zhu *et al.*, "A 3D interpolation method in repairing hand vascular tree for vein recognition," in *Proc. IEEE Int. Conf. Imag. Syst. Techn. (IST)*, Oct. 2013, pp. 254–258.
- [38] E. A. Jones, F. le Noble, and A. Eichmann, "What determines blood vessel structure? Genetic prespecification vs. Hemodynamics," *Physiology*, vol. 21, no. 6, pp. 388–395, 2006.
- [39] R. Sanchez-Reillo, C. Sanchez-Avila, and A. Gonzalez-Marcos, "Biometric identification through hand geometry measurements," *IEEE Trans. Pattern Anal. Mach. Intell.*, vol. 22, no. 10, pp. 1168–1171, Oct. 2000.
- [40] A. Baig, A. Bouridane, F. Kurugollu, and G. Qu, "Fingerprint—Iris fusion based identification system using a single Hamming distance matcher," in *Proc. Symp. Bio-Inspired Learn. Intell. Syst. Secur.*, Aug. 2009, pp. 9–12.
- [41] F. Li, M. K. H. Leung, and X. Yu, "Palmprint identification using Hausdorff distance," in *Proc. IEEE Int. Workshop Biomed. Circuits Syst.*, Dec. 2004, pp. S3/3–S3/8.
- [42] Y. Rubner, C. Tomasi, and L. J. Guibas, "The earth mover's distance as a metric for image retrieval," *Int. J. Comput. Vis.*, vol. 40, no. 2, pp. 99–121, Nov. 2000.
- [43] H. P. Schwan, "Engineering in medicine and biology society, 1994. engineering advances: New opportunities for biomedical engineers," in *Proc. IEEE 16th Annu. Int. Conf.*, Nov. 3–6, 1994, pp. 70a–71a.
- [44] Y. Rubner and C. Tomasi, "The Earth mover's distance," in *Perceptual Metrics for Image Database Navigation*. Boston, MA, USA: Springer, 2001, pp. 13–28.
- [45] Z. Ren, J. Yuan, and Z. Zhang, "Robust hand gesture recognition based on finger-earth mover's distance with a commodity depth camera," in *Proc. 19th ACM Int. Conf. Multimedia*, 2011, pp. 1093–1096.
- [46] A. Ross, A. Jain, and S. Pankati, "A prototype hand geometry-based verification system," in *Proc. 2nd Conf. Audio Video Based Biometric Person Authentication*, 1999, pp. 166–171.
- [47] Y. Song, Z. Cai, and Z.-L. Zhang, "Multi-touch authentication using hand geometry and behavioral information," in *Proc. IEEE Symp. Secur. Privacy (SP)*, May 2017, pp. 357–372.
- [48] S. F. Bahgat, S. Ghoniemy, and M. Alotaibi, "Proposed multimodal palm veins-face biometric authentication," *Int. J. Adv. Comput. Sci. Appl.*, vol. 4, no. 6, pp. 92–96, 2013.
- [49] C. Yuan, X. Sun, and R. Lv, "Fingerprint liveness detection based on multi-scale LPQ and PCA," *China Commun.*, vol. 13, no. 7, pp. 60–65, Jul. 2016.
- [50] K. Daoudi *et al.*, "Handheld probe integrating laser diode and ultrasound transducer array for ultrasound/photoacoustic dual modality imaging," *Opt. Express*, vol. 22, no. 21, pp. 26365–26374, 2014.
- [51] K. Sivasubramanian and M. Pramanik, "High frame rate photoacoustic imaging at 7000 frames per second using clinical ultrasound system," *Biomed. Opt. Express*, vol. 7, no. 2, pp. 312–323, 2016.
- [52] T. J. Allen and P. C. Beard, "High power visible light emitting diodes as pulsed excitation sources for biomedical photoacoustics," *Biomed. Opt. Express*, vol. 7, no. 4, pp. 1260–1270, 2016.

Yuehang Wang is currently pursuing the Ph.D. degree in biomedical engineering.

Zhengxiang Li is currently pursuing the Ph.D. degree in computer science and engineering.

Tri Vu is an undergraduate student in biomedical engineering.

Nikhila Nyayapathi is currently pursuing the Ph.D. degree in electrical engineering.

Kwang W. Oh is an Associate Professor of Electrical Engineering.

Wenyao Xu is an Associate Professor of Computer Science and Engineering.

Jun Xia is an Assistant Professor of Biomedical Engineering.